Title

Unraveling the Crystallization Kinetics of 2D Perovskites with Sandwich-Type Structure for High-Performance Photovoltaics

Journal

Advanced Materials, 32(36)

ISSN

0935-9648

Authors

Song, Jingnan

Zhou, Guanqing

Chen, Wei

et al.

Publication Date

2020-09-01

DOI

10.1002/adma.202002784

Peer reviewed

Unravelling the crystallization kinetics of 2D perovskites with sandwich-type structure for high-performance photovoltaics

Jingnan Song, Guanqing Zhou, Wei Chen, Quanzeng Zhang, Jazib Ali, Qin Hu, Jing Wang, Cheng Wang, Wei Feng, Aleksandra B. Djurišić, Haiming Zhu*, Yongming Zhang, Thomas Russell and Feng Liu**

Dr. Jingnan Song,[+] Guanqing Zhou,[+] Quanzeng Zhang, Jazib Ali, Jing Wang, Prof. Yongming Zhang, Prof. Feng Liu
Frontiers Science Center for Transformative Molecules, School of Chemistry and Chemical Engineering, Shanghai Jiao Tong University, Shanghai 200240, China
E-mail: fengliu82@sjtu.edu.cn
Dr. Wei Chen,[+] Prof. Aleksandra B. Djurišić
Department of Physics, University of Hong Kong, Pokfulam, Hong Kong Special Administrative Region
Dr. Qin Hu, Prof. Thomas Russell
Department of Polymer Science and Engineering, University of Massachusetts, Amherst, MA 01003, USA
Materials Sciences Division, Lawrence Berkeley National Laboratory, Berkeley, California 94720, USA
E-mail: qinhu@lbl.gov
Prof. Cheng Wang
Advanced Light Sources, Lawrence Berkeley National Laboratory, Berkeley, California 94720, USA
Wei Feng
State Key Laboratory of Fluorinated Materials, Zibo City, Shandong 256401, China
Prof. Haiming Zhu
Department of Chemistry, Zhejiang University, Hangzhou 310027, China
E-mail: hmzhu@zju.edu.cn
[+]These authors contributed equally to this work.

Keywords: 2D perovskites, sandwich-type structure, *in situ* GIWAXS, crystallization kinetics, high performance

Abstract: Two-dimensional (2D) perovskite solar cells with high stability and high efficiency have attracted significant attention. A systematical static and dynamic structure investigation is carried out to show the details of 2D morphology evolution. A dual additive approach is used, where the synergy between alkali metal cation and polar solvent leads to high quality 2D perovskite films with sandwich-type structures and vertical phase segregation. Such novel structure can induce high quality 2D slab growth and reduce internal and surface defects, resulting in a high device efficiency of 16.48% with enhanced continuous illumination stability, improved moisture (55%-60%) and thermal (85 ^{o}C) tolerances. Transient absorption

spectra reveal the carrier migration from low n to high n species with different kinetics. An $[PbI_6]^{4-}$ octagon coalescence transformation mechanism coupled with metal and organic cations wrapped is proposed. By solvent vapor annealing a recrystallization and reorientation of the 2D perovskite slabs occur to form an ideal structure with improved device performance and stability.

Two-dimensional (2D) organic-inorganic halide perovskites are promising candidates for photovoltaic applications due to an improved balance between efficiency and stability. [1-3] In such materials, lead-iodine slabs are separated by the larger organic cations, forming a structure with general chemical formula of $R_2A_{n-1}M_nX_{3n+1}$, where n is the number of lead-iodine layers between organic cation layers R, such as n-butylammonium (BA^+) and phenethylammonium (PEA^+). [4-6] The hydrophobic spacer cations prevent moisture invasion into the perovskite crystal lattice, delivering devices with robust environmental stability. However, the electrical insulation of organic cation layers significantly impacts the crystallinity and charge transfer, resulting in poor device performance. [7, 8] High-performance 2D perovskites need to align the lead-iodine slabs normal to the substrates, forming vertical pathways that enable efficient charge transport. Efforts have been devoted to enhance the crystal orientation, [1, 9-12] improve the surface quality and crystal size, [13] as well as reduce the nonradiative recombination centers, [14, 15] that have resulted in remarkable improvement in the efficiency and stability of 2D perovskite devices.

Although success has been achieved in elevating device efficiency and stability, precise control of the nanostructure in perovskite film requires a thorough understanding of the crystallization kinetics and the formation mechanism of morphology. Such necessity shaped the current work, in which we introduced alkali metal (KI) and a polar solvent (DMSO) additive to guide the crystal growth and morphology evolution in 2D perovskite film. Grazing-incidence wide-angle x-ray scattering (GIWAXS) experiments provided details on

the phase transition and vertical alignment of 2D perovskite films. The 2D perovskite thin film crystallization follows a nano-cage transformation mechanism with poor orientation and crystallinity upon casting. Subsequent solvent vapor annealing leads to a reorganization of the perovskite film, an increase of the crystalline grains, and a redistribution of the metal and organic cations to form a better-defined 2D structure with improved orientation and crystallinity. More importantly, a sandwich-type metal cation vertical segregation was uncovered in the 2D perovskite film, with K^+ enrichment at both top and bottom interfaces. This structure of the film passivates internal defects, and improves both anode and cathode contacts, leading to drastically improved carrier diffusion length and faster transport kinetics. With this active layer structure, the power conversion efficiency (PCE) reached 16.48%, along with improved operational stability under continuous illumination and enhanced tolerance to humidity (55%-60%) and thermal (85 ^oC) stress. The current research reshapes the understanding of 2D perovskite formation mechanism, and introduces a new structural feature that enhances device performance and stability.

GIWAXS measurements were performed to determine the crystal structure and orientation of perovskite thin films. As shown in **Figure 1a**, the film without additives (control) showed scattering rings, suggesting a random crystal orientation. Diffraction spots were also observed characteristics of a 2D crystal orientation. DMSO additive markedly improved the crystal alignment, as evidenced by the intensification and sharpening of the diffraction spots, though a weak diffuse scattering was still evident (**Figure 1b**). Using both KI and DMSO as additives, denote DAP or dual additive processing, only discrete, sharp Bragg spots were evident, indicating that DAP promoted the unit cell orientation and vertical growth of the 2D crystals, enabling efficient charge transport and extraction in the vertical direction (**Figure 1c**). The Miller indices in **Figure 1c** were indexed using a simulated diffraction pattern from the CIF file of the single crystal $BA_2MA_3Pb_4I_{13}$. [16] It is apparent that the growth direction of perovskite is mainly along the (101) plane that parallel to the substrate,

as indicated in **Figure S1**. The orientation improvement was further evidenced by the 45° line-cut profiles (**Figure S2a**) and pole figures (**Figure 1d** and **Figure S3**). Pole figures of $[PbI_6]^{4-}$ cubic lattice packing were integrated from 0.96-1.04 $Å^{-1}$. The improved 90° chi-angle intensity and a low flat base line indicated improved crystal orientation for DAP based 2D perovskite films (90° chi-angle denotes the out-of-plane direction). The quantitative orientation distribution can be described by an orientational order parameter *S*, given by: [17, 18]

$$S = \frac{1}{2}(3f - 1) \tag{1}$$

$$f = \int_0^{\frac{\pi}{2}} (\cos x)^2 f(x) dx \tag{2}$$

where *f* is the orientation of the $[PbI_6]^{4-}$ octagon normal to the substrate, determined from the azimuthal dependence of the scattering intensity *f* (x) (see the **Supplementary note 1**). *S* for the control sample is 0.57, indicating a near random orientation. In DMSO case, an *S* value of 0.95 was obtained, reflecting a markedly improved orientation, and with DAP a value of 0.98, near perfect orientation of the 2D perovskite slabs is obtained. The 2D scattering patterns was reduced to 1D profile through circular average mode that best assesses crystalline information. As shown in 1D profiles (**Figure S2b**) and peak fitting results of perovskite phase at q=1.0 $Å^{-1}$ (**Figure 1e**), the 2D perovskites with additives showed enhanced peak intensity and enlarged crystal size. The detailed structural information, shown in **Figure S4** and **S5**, further confirmed that DMSO and KI dual additives work synergistically to enhance crystallinity and unit cell orientation in 2D perovskite film, forming vertical pathways to facilitate charge transport. GIWAXS of different incident angles, 0.2 ° and 0.5 °, was used to detect the crystalline information of near surface region and bulk domain for DAP thin film. The lattice strain was calculated using a modified Willliamson-Hall method. [19-21] The lattice strain is 5.6% at the near surface region, and notably reduces to 3.2% when x-ray goes deeper,

suggesting an inhomogeneous distribution of the vertical nanostructure, which is subject to further characterizations.

The thin film morphology was investigated using scanning electron microscopy (SEM) and atomic force microscopy (AFM) to probe the formation mechanism of the morphology (**Figure S6**). As shown in **Figure S7**, the control sample showed irregularly packed crystalline stems, corresponding to the random crystal orientation in GIWAXS. DMSO additive converted the crystal stems into flakes, forming a smoother surface topography. With DAP, smoother surfaces with larger grain sizes are evident, giving rise to improved device performances. However, it should be noted that the amount of KI in the DAP must be carefully controlled. As seen in **Figure S8**, increasing the amount of KI slightly leads to flat cubic crystal stalks aligned normal to the film surface. Time-of-flight secondary-ion mass spectroscopy (ToF-SIMS) was used to investigate the distribution of components normal to the film surface (**Figure 1g**). The perovskite films were covered with a thin polystyrene (PS) layer, so that a constant sputtering rate could be achieved before entering into the perovskite layer. Pb^{2+}, $CH_3NH_3^+$, K^+ signals were recorded as a function of time. In the control film, the rough surface causes a convolution of the actual Pb^{2+} and $CH_3NH_3^+$ depth profile with the profile of the surface topography. The slight Pb^{2+} and $CH_3NH_3^+$ depletion at ~100 s may arise from a surface enrichment of organic cations that not yet formed crystalline structure. The DMSO processed thin film appear to have reduced amounts of Pb^{2+} and $CH_3NH_3^+$ at the surface, though this is artefactual and arises from the surface roughness, and the concentration of components is uniform as a function of depth. DAP thin film showed interesting vertical segregation that the film surface and bottom were enriched with K^+, forming a sandwich structure with two sides enclosed by the metal cation induced 2D crystals. Such a unique stratification could be attributed to the preferential interaction of K^+ with the substrate and air interface, which could be explained by Marangoni convection. [22] This sandwiched structure

provides new insights of charge carrier kinetics and structure manipulation for perovskite based optoelectronic devices.

To assess the excitonic properties and carrier transport dynamics in the perovskite films, steady state and transient optical spectra were obtained. **Figure S9a** shows the normalized UV-vis absorption spectra of 2D perovskite films. Well-resolved absorption peaks at 566, 602, and 635 nm are seen in the DAP samples, which are assigned to the excitonic absorption of the 2D perovskite with n values of 2, 3, and 4. Thus multiple 2D perovskite phases with different slab thickness coexist in the film, which is in good agreement with previous reports. [14, 23] The difference between the front- (perovskite film) and back- (glass) excited photoluminescence (PL) spectra in **Figure S9b-d** show the inhomogeneity of the 2D perovskite phase distribution, where small-n phases are enriched on the glass side and large-n phases are preferentially located on top of the film. Transient absorption (TA) measurements were conducted to further investigate the distribution of 2D and 3D phases and the dynamics of charge carriers in the perovskite thin films. [23-26] Shown in **Figure S10a-c** and **Figure 2a-c** were the 2D TA color plots collected by exciting the 2D perovskite films from the front side and back side, respectively. For control sample, the front-excited TA spectra were dominated by the ground-state bleaching (GSB) of n≈∞ phase (3D perovskites), as shown in the gray line of **Figure 2d**. In comparison, the back-excited TA spectra showed four distinct GSB peaks at 575 nm (n=2), 610 nm (n=3), 630 nm (n=4), and 705 nm (n≈∞). The sharp contrast between back-excited and front-excited TA spectra suggest that the 2D perovskite phases were readily aligned with a higher concentration of low-n phases at the bottom and n≈∞ phases near the surface in perovskite film, [23] which is in agreement with the PL results. The contrast is further enhanced as the DMSO additives were added. The front-excited TA spectra of 2D perovskite film exhibit photo-bleaching (PB) peaks at 612 nm (n=3), 644 nm (n=4), and 692 nm (n=5) in conjunction with that of n≈∞, which is similar to the back-excited TA spectra except intensity variations. Thus DMSO increased the 2D perovskite concentration at both the

top and bottom interfaces in comparison to the control samples. KI can further increase the concentration of low-n perovskite phases at the DAP film surface, as evidenced by the increased PB peak intensity of low-n species and reduced intensity of n≈∞ species in front-excited TA spectra.

The photoexcitation energy transfer kinetics in 2D perovskite films were further analyzed. Representative TA spectra at different decay times and TA kinetics at different wavelengths corresponding to different components are shown in **Figure 2d-i** (back side excitation) and **Figure S10d-f** (front side excitation). In all three cases, upon photoexcitation from the back side, the GSB signals of low n 2D phases form in ultrafast timescale (< 0.5 ps) and subsequently show a fast decay in 1 ps and a slow decay in 100 ps. The decay of GSB signal of low n phases is accompanied by the rise of GSB signal of n≈∞, indicating that photoexcitation energy in 2D layers could transfer to the n≈∞ component. [23, 27] The fast component and slow component can be assigned to energy transfer and charge transfer process, respectively. [28] Further decay at longer time scales (>100 ps) is associated with carrier recombination process (e.g. radiative recombination). [29] We note there is negligible photoexcitaiton energy transfer for n=5 phase to n≈∞ component in DMSO and DAP samples, which could be due to the small driving force. A careful examination on early time ultrafast process in different 2D layers show faster rise and decay times with smaller n, suggesting energy transfer from smaller n to larger n but finally ends up in n≈∞ component. The transfer lifetimes between 2D phases were extracted by fitting the TA kinetics of low n phases using the exponential function. [29] The fast decay lifetime (τ_1) for control, DMSO, and DAP samples were 0.30±0.008, 0.40±0.021, 0.58±0.013 ps, respectively. Such an increase in time scale is in good agreement with crystal size increase, corresponding to a distance that the exciton must go through to reach other species. Further, we fit the rising kinetics (n=∞, back excitation) of control, DMSO, DAP samples and the corresponding lifetimes are 32.53±2.54,

28.85 ± 1.36, 27.78 ± 1.15 ps, respectively. This indicates that additive can enable highly efficient electron transfer from low n to n=∞ due to the better phase distribution and high crystallinity. The transient absorption spectroscopy reveals the vertical segregation of 2D perovskite crystals in thin film, and enhanced charge transporting resulted from the perovskite dimensional engineering. We speculate that, although the DMSO additive can induce better structural order of 2D slabs and passivate some internal defects through crystal reorganization, the high concentration of 3D crystalline species at front side still result in defects at the interface with the hole or electron transporting layer under the stoichiometry constraint. Adding KI as a supplementary additive solves this issue quite effectively. Better vertical segregation of 2D slabs is observed, and KI promoted 2D crystals are enriched at both the top and bottom interfaces. It is expected that the metal cation induced Ruddlesden-Popper crystal would be in a small inter-slab distance, and of low defect density, since organic cations are reduced.

Photovoltaic performances of 2D perovskite solar cells were measured with a planar heterojunction structure of ITO/PEDOT:PSS/$BA_2MA_3Pb_4I_{13}$/PCBM/BCP/Ag (**Figure S11**). **Figure 3a** shows the photocurrent density-voltage (*J*-*V*) curves, and the corresponding device parameters are summarized in **Table 1**. Solar cells based on control films show a poor PCE of 10.37% with low short-circuit current density (J_{SC}), open-circuit voltage (V_{OC}), and fill factor (FF). Such poor device performance was ascribed to the poor charge transport imposed by the random crystal orientation and high defect density in the control film. For the DMSO based 2D perovskite solar cell, a higher PCE of 12.97% was achieved with improved J_{SC}, FF, and V_{OC}. For DAP based device, a champion device gave a PCE of 16.48% with a V_{OC} of 1.18 V, J_{SC} of 18.67 mA cm^{-2} and FF of 74.80%. The PCE is consistent with that obtained from the steady-state power output measurements by holding a voltage at the maximum power point shown in **Figure S12** and the J_{SC} is matched with that integrated from the external quantum efficiency (EQE) data shown in **Figure S13**. Moreover, negligible photocurrent hysteresis can

be observed in the DAP based devices, as indicated by the similar *J-V* curves under reverse and forward scans (**Figure S14**). The amount of additive has a strong influence on the device performance, with detailed results shown in **Figure S15** and **Table S1**. To confirm the reproducibility of our device efficiency, we fabricated 20 devices for each case, which showed average PCE of 9.75% for control device, 12.33% for DMSO based device, and 15.07% for DAP based device (**Figure S16**). Except enhanced device efficiency, a series of stability tests were carried out under various conditions, with results shown in **Figure 3b** and **Figure S17**. The upper figure in **Figure 3b** shows the continuous illumination stability operated at maximum power point (MPP, 0.83 V for control and 0.98 V for DAP) in an ambient environment (55%~60% RH) under continuous 1 sun illumination. The control device degrades to 40.3% of its initial PCE after 3200 min continuous illumination. In contrast, the DAP device retained ~80%, suggesting significantly improved operational stability at continuous working conditions. Moreover, the DAP based devices show higher tolerance to humidity and thermal stress. After 34 days tracking, the DAP based device maintains ~89% of its initial value after exposing to the ambient condition with humidity of 55%-60% and ~91.6% after continuous heating at 85 ^{o}C, which are higher than the control one. These results demonstrate that the sandwich-type of structure of the perovskite induced by DAP processing can promote both the efficiency and device stability.

Shown in **Figure S18** were the dark *J-V* curves of devices processed with different additives. The significantly reduced reverse dark current suggested that additives could prevent leakage current. The improved forward current levels at high voltages indicate good injection and transport in perovskite layers. The voltage-dependent ideality factor n can be derived from the dark *J-V* curves according to the following equation, [30] with results shown in **Figure 3c**.

$$\mathrm{n} = \frac{q}{kT}\frac{dV}{d\ln J_d} \tag{3}$$

where n is the ideality factor, J_d is the dark current. The actual ideality factor refers to the plateau value in the n-V curves. For the control and DMSO processed thin films, the ideality factor is 3.20 and 2.52, respectively. Such large ideality factor suggests that the multi-level traps induced defects coupling effect complicated the recombination processes. [31-33] For the DAP samples, the ideality factor is 1.58, suggesting shallow traps induced Shockley-Read-Hall recombination. [34] The significantly reduced ideality factor after additive treatment suggested the decreased nonradiative recombination, especially for the DAP case due to its novel sandwich structure. Furthermore, space charge limited current (SCLC) measurements were conducted on electron-only devices (ITO/SnO_2/$BA_2MA_3Pb_4I_{13}$/PCBM/BCP/Ag), with results shown in **Figure 3d**. The trap density was determined by the trap-filled limit voltage using the following equation: [35, 36]

$$N_t = \frac{2V_{TFL}\varepsilon_r\varepsilon_0}{qL^2} \quad (4)$$

Where V_{TFL} is the onset voltage of the trap-filled limited region, ε_0 is the vacuum permittivity, ε_r is the relative dielectric constant, and L is the thickness of the film. The calculated trap density for control, DMSO, and DAP films is 3.51×10^{16} cm^{-3}, 2.41×10^{16} cm^{-3}, and 1.92×10^{16} cm^{-3}, respectively. The reduced trap density in DAP film is attributed to dual sides passivation of sandwich-type perovskite structure, and expected to account for the enhanced fill factor and V_{OC} in the photovoltaic devices. This is also in good agreement with the TA spectra analysis that the sandwich-type perovskite structure can improve charge carrier transport and collection, delivering enhanced device efficiency and long-term stability. The device characteristics, together with structure and TA characterization, showed the significant advantage of the sandwich-type perovskite solar cells. As shown in **Figure 3e**, the DAP devices exhibit a sandwich-type distribution of potassium iodide (K^+), thereby effectively passivating the defects at interfaces of electron-transporting layer (ETL)/perovskite film and

hole-transporting layer (HTL)/perovskite film and suppressing the trap-assisted recombination, yielding improved device parameters.

The dynamics of carrier recombination and extraction were further explored using time-resolved photoluminescence (TRPL) spectra on bare perovskite films and heterojunctions with PCBM layer (**Figure S19** and **Table S2-S3**). Bare perovskite films displayed a longer average carrier lifetime (τ_{ave}) of 2.25, 3.31, 10.07 ns for control, DMSO, and DAP films. The extended carrier lifetime indicates the elimination of nonradiative recombination arising in the 2D perovskites, attributing to the additive-induced defects passivation. The PL lifetime were substantially reduced when the perovskite films were covered with PCBM layer, with fitted lifetimes of 2.09, 1.91, and 1.58 ns for control, DMSO, and DAP films. Thus, more efficient quenching was achieved in DAP thin film, suggesting a more efficient charge carrier extraction at the perovskite/PCBM interface. Following the 1D diffusion equations (see the **Supplementary Note 2**), the carrier diffusion length (L_D) could be expressed as follows. [37-39]

$$L_D \approx \frac{2d}{\pi}\sqrt{2\left(\frac{\tau}{\tau_{quench}}-1\right)} \quad (5)$$

where d is the thickness of perovskite film, τ is the carrier lifetime, and τ_{quench} is quenched lifetime. The diffusion lengths are 61, 204, 542 nm for control, DMSO, and DAP films (**Table S4**). Carrier diffusion is associated with crystalline order and defects density, thus the sandwich-type structure in DAP thin film can substantially improve these parameters to create superb pathways for long distance charge transport, resulting in enhanced device performance.

In situ GIWAXS experiments were conducted to monitor the drying process of slot-die printed perovskite film to capture the crystallization kinetics. A series of representative 2D GIWAXS images at different drying stages are provided in **Figure S20** and **Supplementary Videos 1-3**. The 1D intensity-time profiles were summarized in **Figure S21**, and 2D color mapping of *in situ* GIWAXS results as well as the corresponding peak intensity analysis are shown in **Figure 4**. In all three cases, the scattering feature seen at high q values (~1.5 $Å^{-1}$) in

early stage is associated with the interdistance of solvent molecules. Another common feature is the scattering halo at low q values (~0.4 $Å^{-1}$), which is associated with $[PbI_6]^{4-}$ cage distance. As time elapsed, these two broader peaks gradually shifted to higher q values, suggesting the evaporation of free DMF solvent and formation of ordered intermediate phases, which is similar to the 3D perovskites crystalline evolution. [40-42] However, the $[PbI_6]^{4-}$ assembly stabilized at q≈0.5 $Å^{-1}$, which differs from 3D crystal formation (q≈0.6 $Å^{-1}$). [43] The enlarged $[PbI_6]^{4-}$ interdistance is attributed to the trapping of large sized organic cations. Subsequently, a structure transformation from $[PbI_6]^{4-}$ assembly to crystals were observed. For the control case, the transformation from $[PbI_6]^{4-}$ assembly to perovskite phase (q=1.0 $Å^{-1}$) happened at ~100 s, which is slower in comparison to the additive processed cases (~70-60 s), as seen from the red dash bars in 2D color mapping. Such result is expected since DMSO is more readily incorporated into the perovskite crystals and, therefore, should be in close contact with the $[PbI_6]^{4-}$ octagon and expel DMF out to promote early crystallization. We see that DMSO additive processed film showed a quite narrow transition zone, which confirmed such a process. Further increasing drying time, sharp peaks at around 0.47, 0.31, and 0.23 $Å^{-1}$ appeared, corresponding to the low-n 2D phases (n=1, 2, and 3), respectively. They developed together during the structure transformation. The DAP processing leads to an obvious difference than the DMSO case where the low-n phase peak is much stronger and sharper (**Figure 4e-f**). Thus better quality and larger quantity 2D crystals are formed. Such feature can be traced back to crystallization process. In DAP case, a wider transition zone was seen, and a small tail of q=1.0 $Å^{-1}$ peak was observed and lasted for a long period, and then quickly got intensified in late transition zone. In the early stage of the transformation this can be viewed as a seeding process that induces better crystal quality and higher crystallinity in the resultant thin film, due to the addition of KI that counter balances the DMSO associated crystallization effect. It should be noted that the as cast 2D perovskite films have poor crystal orientation since the rapid drying can result in many structural defects. The detailed film drying versus

peak intensity plots showed the important structure transitions that can be used to evaluate the content of low n species. The n≈∞ peak intensity summaries 3D crystal as well as the 2D perovskite $[PbI_6]^{4-}$ distance. The intensity ratio of low n peak to n≈∞ peak revealed the low n species concentration. And in this case, DAP film yielded the highest low n species concentration.

We then carried out *in situ* solvent vapor annealing (SVA) experiments to recrystallize and reorient the best performing DAP films. [44-46] Important 2D diffraction images are shown in **Figure 5a** and **Supplementary Video 4**. It can be seen that the low n species diffraction peaks that are below 0.7 $Å^{-1}$ gradually get narrowed toward the out-of-plane direction and form an intermediate state at around frame 100. Then, the n=1 and 2 2D crystals transformed to higher n species rapidly, indicating that the low n crystal is less stable in comparison to the high n ones. Consequently, the high n species in the out-of-plane direction disappeared with the Bragg spots intensified, indicating the reorientation of the 2D slabs. (The broad scattering ring at q~0.4 $Å^{-1}$ occurring in the third panel of **Figure 5a** is due to the characteristic signal of Kapton windows mentioned in the experimental section) It should be noted that no 2D diffraction peak was seen in in-plane direction. Such results indicate that although the vertical growth and orientation of 2D perovskite crystals were improved, they cannot form long-range ordered structures, as reported in previous literatures. [11, 47] They appear to form unit cell orientation. The 1D out-of-plane line-cut profile and pole figures were provided in **Figure S22** and **Figure S23**, and 2D color mapping of *in situ* SVA process as well as the corresponding peak intensity analysis are shown in **Figure 5b-c**. The difference in line bars clearly showed the transformation sequence of low n crystal to high n crystals. And in high q region around q=2 $Å^{-1}$, the background was much lower in comparison to the as cast film (**Figure S21**). Thus, the overall crystallinity was improved by SVA treatment by inducing crystallization of the kinetically trapped amorphous materials and assemblies.

In situ film drying and SVA experiments provide important morphology formation details that can be used to construct a structure evolution model (**Figure 5d**). Perovskite in solution forms $[PbI_6]^{4-}$ octagons that are surrounded by organic cations and solvent shells. Solvent evaporation leads to $[PbI_6]^{4-}$ octagon self-assembly that can be transformed into 2D and 3D perovskites by coalescence of $[PbI_6]^{4-}$ octagon. Metal and organic cations will be trapped inside or diffuse out to form boundaries to prohibit further $[PbI_6]^{4-}$ octagon coalescence gauged by the stoichiometry of MA^+, metal and BA cations. A certain amount of BA cation trapped $[PbI_6]^{4-}$ octagons will be deposited in the amorphous form and, therefore, the as-cast thin film is in random orientations and with low crystallinity. As the perovskite films are exposed to a DMF atmosphere, the solvent molecules will penetrate into the perovskite films, and dissolve disordered and less stable low n species. Further thermal annealing treatment can contribute to redistribution of metal and organic cations, and reorganize the 2D slabs into a vertical orientation. DMSO could get incorporated in $[PbI_6]^{4-}$ octagon to control crystal transformation due to its strong interaction with $[PbI_6]^{4-}$ octagon and forms typical q=0.4 $Å^{-1}$ diffraction in perovskite film (**Figure S21**). Alkali metal cation peel of DMSO skin to interact with $[PbI_6]^{4-}$ octagon, similar to the function of Cs, [48] leading to reduced q=0.4 $Å^{-1}$ intensity and enhanced 2D peak intensity, bringing better quality crystalline film. Alkali metal cation also induces new structure features, such as q=0.5 $Å^{-1}$ and q=0.65 $Å^{-1}$ peaks, which could be attributed to the slab-to-slab distance with a metal cation kink, which is important to inter slab charge transport since much larger carrier diffusion length were seen. Solvent vapor annealing leads to improved structure order of perovskite film by redistribute metal and organic cations and reorient 2D slabs. The vertical segregation of KI at bottom and top interfaces results in a sandwich-type of 2D crystal that has good carrier transport and collection, giving rise to improved device performances.

To conclude, we developed a novel sandwich-type 2D perovskite aided by the synergy of alkali metal cations and a polar solvent for high-performance solar cells. With such a structure,

nonradiative recombination was substantially inhibited and charge extraction efficiency was significantly improved, resulting in a striking increase in the electron diffusion length and a high efficiency of 16.48%. *In situ* structure characterization was performed to understand the evolution of morphology, from which a detailed picture of the 2D perovskite crystallization was obtained. The $[PbI_6]^{4-}$ octagon coalescence is the major structure formation at an intermediate state that needs to be carefully manipulated to refine the 2D perovskite structure. DMSO additive, alkali metal and organic cations are heavily involved in structure formation, leading to different morphologies at different contents and concentrations. Solvent vapor annealing is critical in improving thin film crystalline order and crystal orientation. The optimized sandwich-type perovskite leads to improved carrier transport and reduces internal and surface defects, giving rise to V_{OC}, J_{SC} and FF simultaneously for the photovoltaic devices. The studies reveal the mystery of 2D perovskite structure formation and controlling mechanism in detail, which paves the way for future 2D perovskite device fabrication and further optimization.

Experimental Section
See experimental details in the Supporting information.

Supporting Information
Supporting Information is available from the Wiley Online Library or from the author.

Acknowledgements

Jingnan Song, Guanqing Zhou, and Wei Chen contributed to this work equally. This work was financially supported by the Young 1000 Talent Program of China, the National Natural Science Foundation of China (NSFC) (Nos. 51973110, 21734009, 21905102, and 61805138), beamline 7.3.3 and 11.0.1.2 at the Advanced Light Source, Lawrence Berkeley National Laboratory, which was supported by the DOE, Office of Science, and Office of Basic Energy Sciences. Q. H. and T. P. R. were supported by the US Office of Naval Research under contract N00014-17-1-2241.

Received: ((will be filled in by the editorial staff))
Revised: ((will be filled in by the editorial staff))
Published online: ((will be filled in by the editorial staff))

References

[1] H. Tsai, W. Nie, J. C. Blancon, C. C. Stoumpos, R. Asadpour, B. Harutyunyan, A. J. Neukirch, R. Verduzco, J. J. Crochet, S. Tretiak, L. Pedesseau, J. Even, M. A. Alam, G. Gupta, J. Lou, P. M. Ajayan, M. J. Bedzyk, M. G. Kanatzidis, *Nature* **2016**, *536*, 312.

[2] H. Lai, B. Kan, Liu, T. Zheng, N. Xie, Z. Zhou, T. Wan, X. Zhang, X. Liu, Y. Chen, *J. Am. Chem. Soc.* **2018**, *140*, 11639.

[3] S. Ahmad, P. Fu, S. Yu, Q. Yang, X. Liu, X. Wang, X. Wang, X. Guo, C. Li, *Joule* **2018**, *3*, 1.

[4] X. Zhang, G. Wu, W. Fu, M. Qin, W. Yang, J. Yan, Z. Zhang, X. Lu, H. Chen, *Adv. Energy Mater.* **2018**, *8*, 1702498.

[5] J. Hu, I. W. H. Oswald, S. J. Stuard, M. M. Nahid, N. Zhou, O. F. Williams, Z. Guo, L. Yan, H. Hu, Z. Chen, X. Xiao, Y. Lin, Z. Yang, J. Huang, A. M. Moran, H. Ade, J. R. Neilson, W. You, *Nat. Commun*. **2019**, *10*, 1276.

[6] G. Wu, J. Zhou, J. Zhang, R. Meng, B. Wang, B. Xue, X. Leng, D. Zhang, X. Zhang, S. Bi, Q. Zhou, Z. Wei, H. Zhou, Y. Zhang, *Nano Energy* **2019**, *58*, 706.

[7] I. C. Smith, E. T. Hoke, D. Solis-Ibarra, M. D. McGehee, H. I. Karunadasa, *Angew. Chem.* **2014**, *53*, 11232.

[8] D. H. Cao, C. C. Stoumpos, O. K. Farha, J. T. Hupp, M. G. Kanatzidis, *J. Am. Chem. Soc.* **2015**, *137*, 7843.

[9] N. Zhou, Y. Shen, L. Li, S. Tan, N. Liu, G. Zheng, Q. Chen, H. Zhou, *J. Am. Chem. Soc.* **2018**, *140*, 459.

[10] C. M. M. Soe, W. Nie, C. C. Stoumpos, H. Tsai, J.-C. Blancon, F. Liu, J. Even, T. J. Marks, A. D. Mohite, M. G. Kanatzidis, *Adv. Energy Mater.* **2018**, *8*, 1700979.

[11] A. Z. Chen, M. Shiu, X. Deng, M. Mahmoud, D. Zhang, B. J. Foley, S.-H. Lee, G. Giri, J. J. Choi, *Chem. Mater.* **2019**, *31*, 1336.

[12] M. Z. Long, T. K. Zhang, D. C. Chen, M. C. Qin, Z. F. Chen, L. Gong, X. H. Lu, F. Y. Xie, W. G. Xie, J. Chen, J. B. Xu, *ACS Energy Lett*. **2019**, *4*, 1025.

[13] X. Zhang, X. Ren, B. Liu, R. Munir, X. Zhu, D. Yang, J. Li, Y. Liu, D.-M. Smilgies, R. Li, Z. Yang, T. Niu, X. Wang, A. Amassian, K. Zhao, S. Liu, *Energy Environ. Sci*. **2017**, *10*, 2095.

[14] J. Qing, X. Liu, M. Li, F. Liu, Z. Yuan, E. Tiukalova, Z. Yan, M. Duchamp, S. Chen, Y. Wang, S. Bai, J.-M. Liu, H. J. Snaith, C. S. Lee, T. C. Sum, F. Gao, *Adv. Energy Mater.* **2018**, *8*, 1800185.

[15] W. Fu, J. Wang, L. Zuo, K. Gao, F. Liu, D. S. Ginger, A. K. Y. Jen, *ACS Energy Lett.* **2018**, *3*, 2086.

[16] C. C. Stoumpos, D. H. Cao, D. J. Clark, J. Young, J. M. Rondinelli, J. I. Jang, J. T. Hupp, M. G. Kanatzidis, *Chem. Mater.* **2016**, *28*, 2852.

[17] J. N. Song, M. Zhang, M. Yuan, Y. Qian, Y. Sun, F. Liu, *Small Methods* **2018**, *2*, 1700229.

[18] J. T.,Rogers, K.,Schmidt, M. F.,Toney, G. C.Bazan, E. J. Kramer, *J. Am. Chem. Soc.* **2012**, *134*, 2884.

[19] D. Luo, W. Yang, Z. Wang, A. Sadhanala, Q. Hu, R. Su, R. Shivanna, G. F. Trindade, J. F. Watts, Z. Xu, Y. Tu, Y. Zhang, X. Yang, W. Zhang, R. H. Friend, Q. Gong, H. J. Snaith, R. Zhu, *Science* **2018**, *360*, 1442.

[20] A. Pramanick, X. P. Wang, C. Hoffmann, S. O. Diallo, M. R. V. Jørgensen, X. L. Wang, *Phys. Rev. B* **2015**, *92*, 174103.

[21] Y. Zhao, J. Zhang, *J. Appl. Cryst.* **2018**, *41*, 1095.

[22] S. G. Yiantsios, B. G. Higgins, *Phys. Fluids* **2006**, *18*, 082103.

[23] J. Liu, J. Leng, K. Wu, J. Zhang, S. Jin, *J. Am. Chem. Soc.* **2017**, *139*, 1432.

[24] M. Yuan, L. N. Quan, R. Comin, G. Walters, R. Sabatini, O. Voznyy, S. Hoogland, Y. Zhao, E. M. Beauregard, P. Kanja-naboos, Z. Lu, D. H. Kim, E. H. Sargent, *Nat. Nanotech.* **2016**, *11*, 872.

[25] Q. Y. Shang, Y. N. Wang, Y. G. Zhong, Y. Mi, L. Qin, Y. F. Zhao, X. H. Qiu, X. F. Liu, Q. Zhang, *J. Phys. Chem. Lett.* **2017**, *8*, 4431.

[26] N. Wang, L. Cheng, R. Ge, S. T. Zhang, Y. F. Miao, W. Zou, C. Yi, Y. Sun. Y. Cao, R. Yang, Y. Q. Wei, Q. Guo, Y. Ke, M. T. Yu, Y. Z. Jin, Y. Liu, Q. Q. Ding, D. W. Di, L. Yang, G. C. Xing, H. Tian, C. H. Jin, F. Gao, R. H. Friend, J. P. Wang, W. Huang, *Nat. Photon.* **2016**, *185*, 699.

[27] A. H. Proppe, R. Quintero-Bermudez, H. R. Tan, O. Voznyy, S. O. Kelley, E. W. Sargent, *J. Am. Chem. Soc*. **2018**, *140*, 2890.

[28] R. Q. Bermudez, A. H. Proppe, A. Mahata, P. Todorovic, S. O. Kelley, F. D. Angelis, E. H. Sargent, *J. Am. Chem. Soc.* **2019**, *141*, 13459.

[29] L. Wang, C. McCleese, A. Kovalsky, Y. Zhao, C. Burda, *J. Am. Chem. Soc.* **2014**, *136*, 12205.

[30] T. Kirchzrtz, F. Deledalle, P. S. Tuladhar, J. R. Durrant, J. Nelson, *J. Phys. Chem. Lett.* **2013**, *4*, 2371.

[31] O. Breitenstein, J. Bauer, P. P. Altermatt, K. Ramspeck, *Solid State Phenom.* **2009**, *156-158*, 1.

[32] O. Breitenstein, P. Altermatt, K. Ramspeck, A. Schenk, *Proc. 21th Eur. Photovoltaic Solar Energy Conference and Exhibition*, Dresden, **2006**, 625.

[33] A. Schenk, U. Krumbein, *J. Appl. Phys.* **1995**, *78*, 3185.

[34] W. Shockley, W. T. Read, *Phys. Rev.* **1952**, *87*, 835.

[35] T. Niu, J. Lu, R. Munir, J. Li, D. Barrit, X. Zhang, H. Hu, Z. Yang, A. Amassian, K. Zhao, and S. Liu, *Adv. Mater.* **2018**, *30*, 1706576.

[36] J. Qiu, Y. Zheng, Y. Xia, L. Chao, Y. Chen, W. Huang, *Adv. Func. Mater.* **2018**, 1806831.

[37] G. Xing, N. Mathews, S. Sun, S. S. Lim, Y. M. Lam. M. Gratzel, S. Mhaisalkar, T. C. Sum, *Science* **2013**, *342*, 344.

[38] S. D. Stranks, G. E. Eperon, G. Grancini, C. Menelaou, M. J. P. Alcocer, T. Leijtens, L. M. Herz, A. Petrozza, H. J. Snaith, *Science* **2013**, *342*, 341.

[39] E. M. Y. Lee, W. A. Tisdale, *J. Phys. Chem. C* **2015**, *119*, 9005.

[40] R. Munir, A. D. Sheikh, M. Abdelsamie, H. Hu, L. Yu, K. Zhao, T. Kim, O. E. Tall, R. Li, D. M. Smilgies, A. Amassian, *Adv. Mater.* **2017**, *29*, 1604113.

[41] D. Barrit, P. Cheng, M.-C. Tang, K. Wang, H. Dang, D.-M. Smilgies, S. F. Liu, T. D. Anthopoulos, K. Zhao, A. Amassian, *Adv. Func. Mater.* **2019**, 1807544.

[42] R. Quintero-Bermudez, A. Gold-Parker, A. H. Proppe, R. Munir, Z. Yang, S. O. Kelley, A. Amassian, M. F. Toney, E. H. Sargent, *Nat. Mater.* **2018**, *17*, 900.

[43] Q. Hu, L. Zhao, J. Wu, K. Gao, D. Luo, Y. Jiang, Z. Zhang, C. Zhu, E. Schaible, A. Hexemer, C. Wang, Y. Liu, W. Zhang, M. Gratzel, F. Liu, T. P. Russell, R. Zhu, Q. Gong, *Nat. Commun.* **2017**, *8*, 15688.

[44] Q. L. Liang, J. G. Liu, Z. K. Cheng, Y. Li, L. Chen, R. Zhang, J. D. Zhang, Y. C. Han, *J. Mater. Chem. A* **2016**, *4*, 223.

[45] K. Meng, L. L. Wu, Z. Liu, X. Wang, Q. F. Xu, Y. D. Hu, S. F. He, X. L. Li, T. Li, G. Chen, *Adv. Mater.* **2018**, *30*, 1706401.

[46] J. Liu, C. Gao, X. L. He, Q. Y. Ye, L. Q. Ouyang, D. M. Zhuang, C. Liao, J. Mei, W. Lau, *ACS Appl. Mater. Interfaces* **2015**, *7*, 24008.

[47] L. Kuai, J. N. Li, Y. J. Li, Y. S. Wang, P. D. Li, Y. S. Qin, T. Song, Y. G. Yang, Z. Y. Chen, X. Y. Gao, B. Q. Sun, *ACS Energy Lett.* **2020**, *5*, 8.

[48] T. Matsui, J. Y. Seo, M. Saliba, S. M. Zakeeruddin, M. Gratzel, *Adv. Mater.* **2017**, *29*, 1606258.

Figures and Figure caption

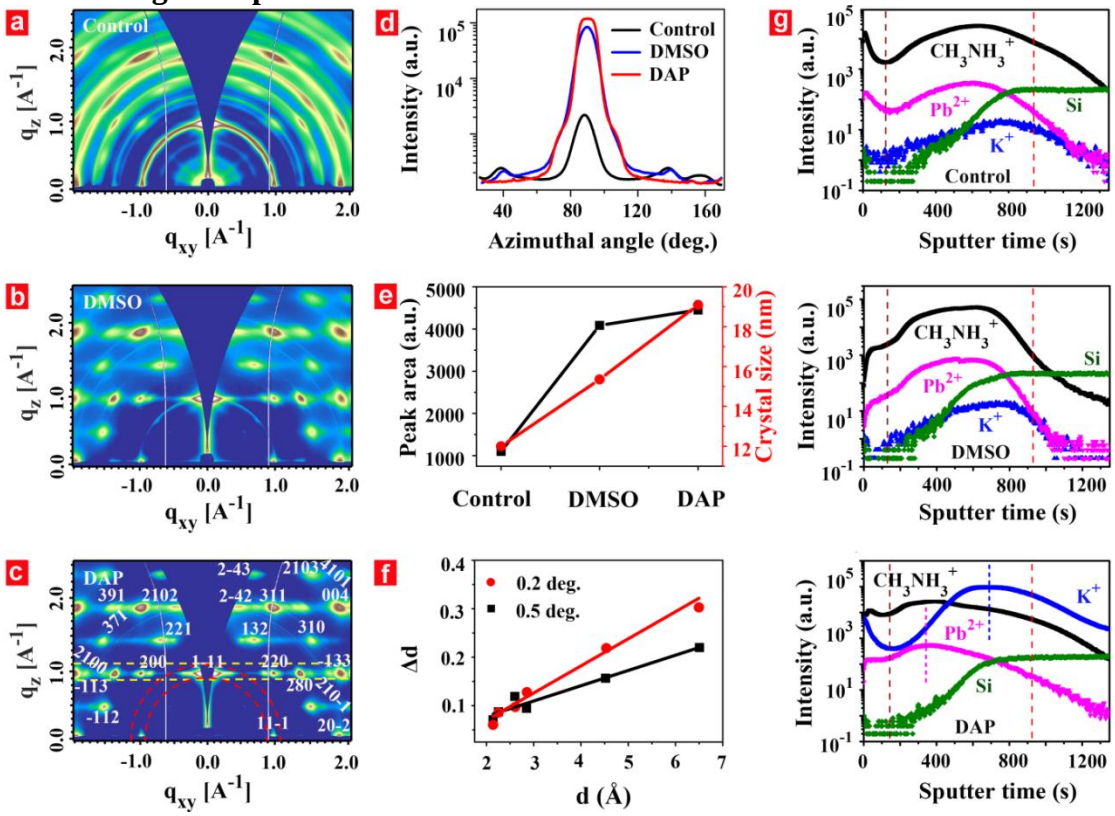

Figure 1. 2D GIWAXS patterns for (a) Control, (b) DMSO, and (c) DAP based perovskite film with Miller indices of the scattering spots shown in white. The Miller indices are indexed using a simulated diffraction patterns from the CIF file of the single crystal $BA_2MA_3Pb_4I_{13}$. (d) Pole figures integrated along the region between red rings shown in c, showing the differences in crystal orientation. Here, 90° chi-angle and 0° chi-angle denote the out-of-plane and in-plane, respectively. (e) The evolution of diffraction area and crystal size of perovskite phase (q=1.0 $Å^{-1}$) as a function of additives. (f) A modified Williamson-Hall plot of Δd versus d spacing extracted from the diffraction profiles with different incident angles. The slopes of the solid lines from linear fits indicate the extents of microstrain at different film thickness. (g) ToF-SIMS depth analysis of control, DMSO- and DAP-processed films.

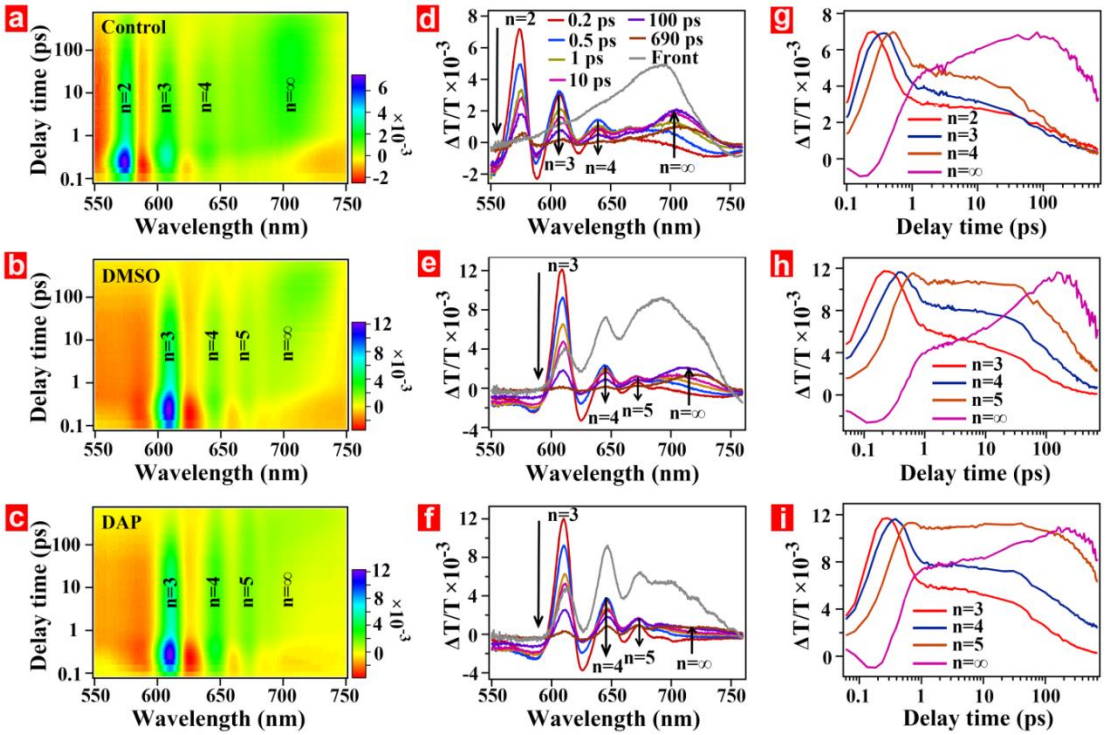

Figure 2. (a-c) 2D color plot of TA spectra for different perovskite films excited from back side (glass) at 400 nm with a fluence below 1 μJ cm^{-2}. (d-f) Representative TA spectra at indicated delay times (Gray lines: TA spectrum excited from front side at 0.5 ps). (g-i) TA kinetics probed at different-n perovskite bands. (a, d, g) Control, (b, e, h) DMSO, and (c, f, i) DAP.

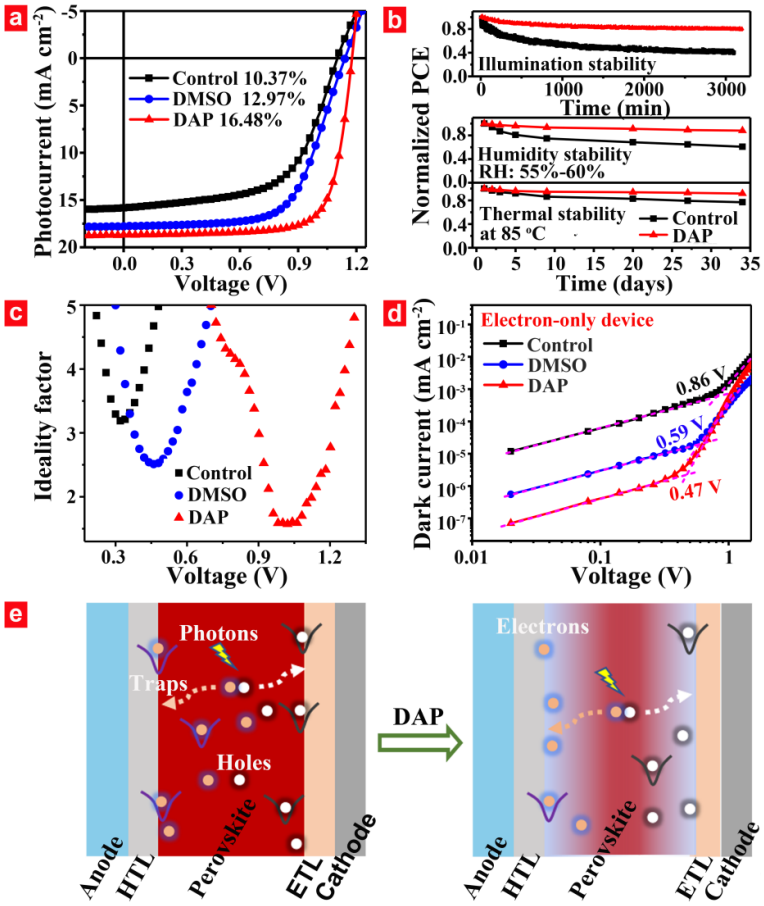

Figure 3. (a) Photocurrent density versus voltage (*J*-*V*) curves of control, DMSO, and DAP based perovskite solar cells. (b) Non-encapsulated device stability measurements of control and DAP based devices under various conditions. Upper figure: continuous illumination stability operated at MPP (0.83 V for control and 0.98 V for DAP) in an ambient environment (55%~60% RH) under continuous 1 sun; middle figure: humidity stability stored in ambient condition with humidity of 55-60%; bottom figure: thermal stability at 85 ^{o}C. (c) Ideality factor as a function of voltage, which were derived from dark *J*-*V* curves. (d) Space charge limited current measurements of the electron-only devices with a structure of ITO/SnO_2/ $BA_2MA_3Pb_4I_{13}$/PCBM/BCP/Ag. (e) Schematic of the trap density reduction for the sandwich-type perovskite structure formed by dual additive process.

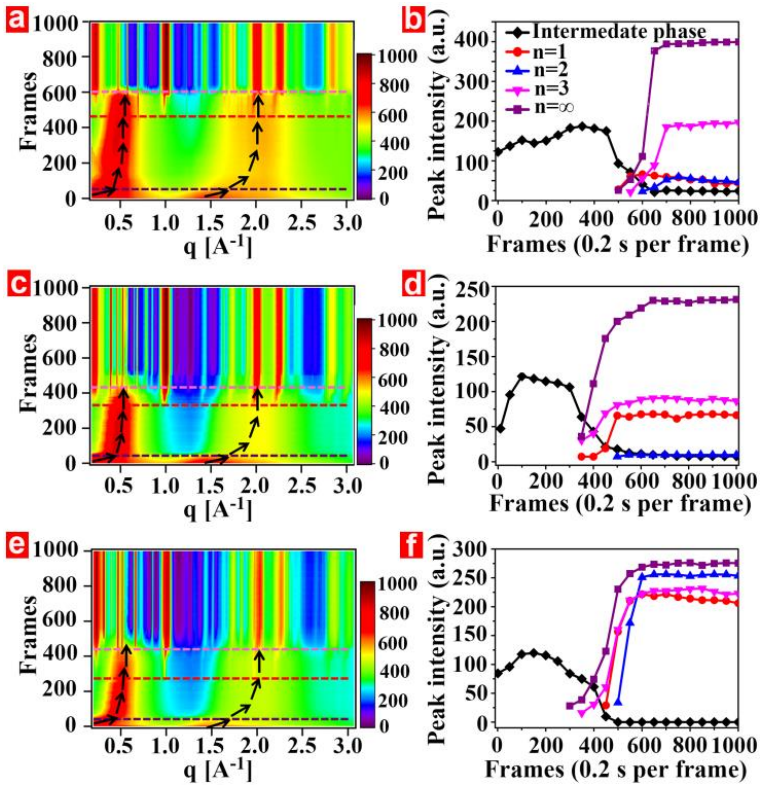

Figure 4. (a, c, e) 2D intensity-time color mappings versus q and frames (0.2 s per frame) for 2D perovskite films fabricated by slot-die printing method. (b, d, f) The corresponding intensity of characteristic peaks, belonging to intermediate phase, different-n perovskite phases (n=1, 2, 3, and ∞), show clear evolution process, suggesting the phase transition from intermediate phase to multiple perovskite phases. (a, b) Control, (c, d) DMSO, and (e, f) DAP.

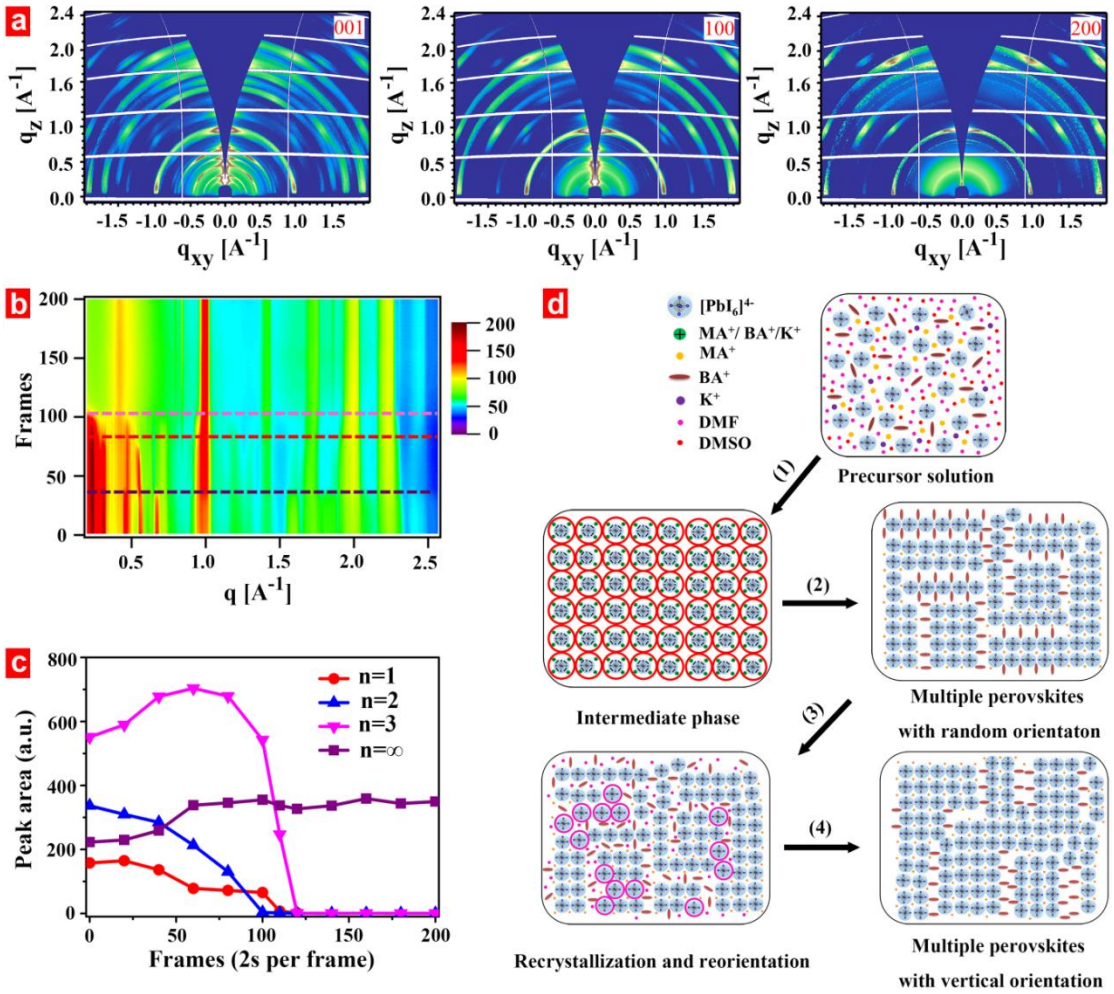

Figure 5. *In situ* solvent vapor annealing (SVA) experiments for DAP-treated 2D perovskites. (a) 2D GIWAXS patterns at different drying stages. (b) 2D intensity-time color mappings versus q and frames (2 s per frame). (c) The evolution of peak intensity derived from its 2D color mappings. (d) The structure evolution model for the formation kinetics of 2D perovskites: (1) Free solvent evaporation to form intermediate phases, (2) Phase transformation from intermediate phases to multiple perovskite phases, (3) SVA treatment to allow recrystallization and reorientation of perovskite phases, (4) Rearrangement of random oriented perovskite phases to form perfectly vertical orientation perovskite phases.

Table 1. Photovoltaic parameters of solar cells based on $BA_2MA_3Pb_4I_{13}$ films processed under different conditions.

Conditions	J_{SC} [mA cm^{-2}]	V_{OC} [V]	FF [%]	PCE [%]
Control	15.83	1.10	59.60	10.37
DMSO	17.77	1.14	63.90	12.97
DAP	18.67	1.18	74.80	16.48

In situ GIWAXS experiment is conducted to reveal the crystallization kinetics and formation mechanism of 2D perovskite films, during which additives play a key role in regulating the nucleation and growth process. For DAP case, a novel sandwich-type structure is achieved, which could effectively passive defects at dual interfaces, finally resulting in a high device efficiency of 16.48%.

Keyword: crystallization kinetics

Jingnan Song, Guanqing Zhou, Wei Chen, Quanzeng Zhang, Jazib Ali, Qin Hu, Jing Wang, Cheng Wang, Wei Feng, Aleksandra B. Djurišić, Haiming Zhu*, Yongming Zhang, Thomas Russell and Feng Liu**

Unravelling the crystallization kinetics of 2D perovskites with sandwich-type structure for high-performance photovoltaics